Structural and Kinetic Effects on Changes in the CO$_2$ Binding Pocket of Human Carbonic Anhydrase II

Dayne West[1], **Chae Un Kim**[3], **Chingkuang Tu**[2], **Arthur H. Robbins**[1], **Sol M. Gruner**[3,4], **David N. Silverman**[1,2,*], and **Robert McKenna**[1,*,†]

[1]Department of Biochemistry and Molecular Biology, University of Florida, Gainesville, FL 32610

[2]Department of Pharmacology and Therapeutics, University of Florida, Gainesville, FL 32610

[3]Cornell High Energy Synchrotron Source (CHESS), Cornell University, Ithaca, NY 14853, USA

[4]Physics Department, Cornell University, Ithaca, NY 14853, USA

Abstract

This work examines the effect on catalysis of perturbing the position of bound CO$_2$ in the active site of human carbonic anhydrase II (HCA II). Variants of HCA II replacing Val143 with hydrophobic residues, Ile, Leu, and Ala, were examined. The efficiency of catalysis in the hydration of CO$_2$ for these variants was characterized by ^{18}O exchange mass spectrometry, and their structures determined by X-ray crystallography at 1.7 to 1.5 Å resolution. The most hydrophobic substitutions V143I and V143L showed decreases in catalysis, as much as 20-fold, while the replacement by the smaller V143A showed only a moderate two-fold decrease in activity. Structural data for all three variants show no significant change in overall position of amino-acid side chains in the active site compared with wild type. However, V143A HCA II showed additional ordered water molecules in the active site compared to wild type. To further investigate the decrease in catalytic efficiency of V143I HCA II, an X-ray crystallographic CO$_2$ entrapment experiment was performed to 0.93 Å resolution. This structure revealed an unexpected shift of the CO$_2$ substrate towards the zinc bound solvent, placing it ~0.3 Å closer than previously observed in wild type in conjunction with the observed dual occupancy of the product bicarbonate, presumably formed during the data acquisition. These data suggest that the Ile substitution at position 143 reduced catalytic efficiency is likely due to steric crowding resulting in destabilization of the transition state for conversion of CO$_2$ into bicarbonate and a decreased product dissociation rate.

The zinc-containing enzyme human carbonic anhydrase II (HCA II) is the most extensively studied of the carbonic anhydrases and is one of the fastest known enzymes, with a maximal
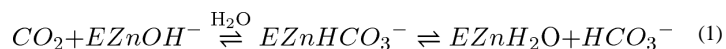
catalytic turnover of 1 μs^{-1} (1-3). HCA II is widely expressed in cells and tissues, contributing to various physiological processes such as acid-base balance, formation of secretory fluids, and respiration (4, 5). The reaction catalyzed by HCA II in a two-stage ping pong mechanism is the reversible hydration of CO_2 to bicarbonate and a proton. In the hydration direction, the first stage is the conversion of CO_2 into bicarbonate via a nucleophilic attack on CO_2 by the reactive zinc-bound hydroxide (eq 1). The resultant bicarbonate is then displaced from the zinc by a water molecule. To regenerate the zinc-bound hydroxide, the active form of the enzyme, a proton transfer reaction occurs (eq 2) between the zinc-bound water and external buffer (B) via the proton shuttle residue His 64 (1-3).

$$CO_2 + EZnOH^- \overset{H_2O}{\rightleftharpoons} EZnHCO_3^- \rightleftharpoons EZnH_2O + HCO_3^- \quad (1)$$

$$EZnH_2O + B \rightleftharpoons EZnOH^- + BH^+ \quad (2)$$

The zinc is centrally located in the active site, bound in a tetrahedral coordination with three histidines (His94, His96, and His119) and a solvent molecule (Figure 1). The active site is partitioned into hydrophobic and hydrophilic surfaces on either side of the zinc ion. On one side is a surface of nonpolar amino acids, Val121, Val143, Leu198, Val207, and Trp209, that form the hydrophobic pocket to which CO_2 binds (6, 7). Detailed crystallographic studies have mapped out the active site of HCA II and demonstrated that one of the oxygen atoms of bound CO_2 interacts with the amide of Thr199 while the other is positioned between the zinc and Val121. This arrangement places the carbon of CO_2 at a distance of 2.8 Å from the oxygen atom of the zinc-bound hydroxide, a position well suited for the nucleophilic attack by the lone pair electrons of the zinc-bound hydroxide oxygen (8, 9) (Figure 1). A well ordered water is also located within the hydrophobic pocket, termed deep water, which is displaced upon binding of CO_2 (Figure 1) (3,6, 7, 10).

On the opposite side of the active site is a region lined with hydrophilic amino acids (Tyr7, Asn62, Asn67, Thr199, and Thr200) primarily responsible for forming the ordered solvent network that is believed necessary to mediating the proton transfer step (1, 11). This network includes five water molecules, the zinc bound water (Zn-W), W1, W2, W3A and W3B, which are stabilized by hydrogen bonds with each other, as well as to hydrophilic side chains (Figure 1). Such a network allows for movement of protons between the zinc-bound solvent and His64 for proton transfer to solution (10) (Figure 1).

Although the binding of CO_2 in the active site of HCA II has been examined by X-ray crystallography (6, 7), the relevance to the catalysis of its position in the enzyme-substrate complex is not well understood. Little is known about the relationship between catalytic efficiency and substrate orientation, a relationship difficult to elucidate experimentally. The work presented here focuses on catalysis by variants of Val143 HCA II and uses X-ray crystallography to elucidate the binding of CO_2 and bicarbonate in the active site of V143I HCA II. There is no significant effect on the structure of ordered waters in the active-site cavity in V143I HCA II, and there are only small effects on rate constants for proton

transfer. However catalysis by V143I HCA II decreased ~20-fold compared with wild type. The larger side chain of Ile143 in V143I presumably decreases the size of the active-site cavity, which results in the CO_2 closer to the zinc by 0.3 Å. This implies a perturbed, crowded transition state which may impede formation of developing charge on product bicarbonate by increased hydrophobicity of Ile143. These structural and kinetic studies elucidate the significance of Val143 and the CO_2 binding site in maximizing catalysis.

MATERIALS AND METHODS

Expression and Purification of Mutants

The position 143 HCA II variants were made by site-directed mutagenesis using an expression vector with a HCA II coding region. Single point mutations were made using the QuikChange II and QuikChange Lightning Kits from Agilent. Verification of mutations was accomplished by DNA sequencing of the entire HCA II coding region, followed by simulated translation using *ExPASY* translate. Expression of mutants involved transformation of mutated plasmid into *Escherichia coli* BL21(DE3)pLysS cells, a cell line specific for protein expression and one that does not express natural CA under experimental conditions. The cells were transformed and expressed at 37°C in LB and enriched 2XYT medium, followed by induction with 1mM isopropyl thiogalactoside when the bacterial growth reached an OD_{600} between 0.6 and 1.2, and the addition of 1mM zinc sulfate to provide a source of zinc for proper folding and functioning of the enzyme. Cells were harvested 4 hrs after induction, spun down, and stored in a −80°C freezer overnight. The cell pellets were lysed and HCA II was purified through affinity chromatography using p-(aminomethyl)benzenesulfonamide (12). Following purification, enzyme concentration was determined by titration with the tight-binding inhibitor ethoxzolamide measuring catalyzed ^{18}O exchange.

Crystallization

Crystals of HCA II variants were obtained using the hanging drop vapor diffusion method (13). The drops were prepared by mixing 5 μL of protein (~10 mg/mL dissolved in 50mM Tris-HCl at pH 8.0) with 5 μL of the precipitant solution (containing 50 mM Tris-HCl at pHs 8, 8.5, and 9 and 1.3 to 1.4 M sodium citrate) against 1 mL of the precipitant solution. The drops were allowed to equilibrate at room temperature. The crystal trays were then stored and allowed to sit undisturbed for one week (13). A crystal of each HCA II variant was cryoprotected by quick immersion into 30% glycerol cryoprotectant solution and flash-cooled by exposure to a gaseous stream of nitrogen at 100K.

CO_2 Binding

CO_2 entrapment experiment for a V143I HCA II crystal was achieved by cryo-cooling (~100K/min) at 15 atm pressure of CO_2 as described in Domsic *et al* (6). A crystal was soaked in a cryo-solution containing 20% glycerol in precipitant solution, then coated with mineral oil and loaded into a high pressure tube. In the pressure tube, the crystal was pressurized with CO_2 gas at 15 atm at room temperature and cryo-cooled to liquid nitrogen without releasing the CO_2 pressure (14).

Data Collection

X-ray diffraction data for the HCA II variants were obtained using an in-house R-AXIS IV[++] image plate system with Osmic Varimax HR optics and a Rigaku RU-H3R Cu rotating anode operating at 50kV and 22 mA. The detector-crystal distance was set to 76 mm. The oscillation steps were 1° with a 5 to 7 min exposure per image. Indexing, integration, and scaling were performed using HKL2000 (15). All three data sets that were collected had an average completeness of > 90% and linear R_{sym} of < 5.0% (Table 1).

Diffraction data for the CO_2 bound V143I HCA II crystal was collected at Cornell High Energy Synchrotron Source (CHESS) F1 beamline using a wavelength of 0.9179 Å. Data were collected in 1° oscillation steps with a 3 s on an ADSC Quantum 270 CCD detector (Area Detector Systems Corp.), with a crystal to detector distance of 100 mm. The detector was offset to cover the high resolution diffraction. The data collected had average completeness of 97.2% and linear R_{sym} of 8.2% (Table 1).

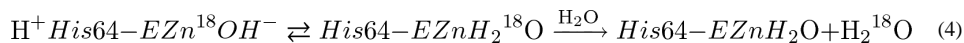### Structure Solution and Model Refinement

All three in house HCA II variants structures were solved using the programs *phaser* and *phenix.refine* in PHENIX (16). Preceding refinement, random test sets of ~5% were flagged for R_{free} calculations. The method of structure determination was molecular substitution (*phaser*) with wild type HCA II (PDB ID: 2ILI) (10). The wild type structure, stripped of the zinc, solvent and amino acid Val 143 replaced with Ala, was used as the initial model for phase calculations in *phenix.refine*. Following 3 cycles in PHENIX, the refined structure was visually inspected using the molecular imaging system Coot for display of model and electron density (17). The zinc, the amino acid substitution at position 143, as well as improperly positioned side chains, were manually placed in their respectively density. This refined model was then submitted for subsequent rounds of refinement and solvent placement. During the final stages of refinement in conjunction with Coot, the models were viewed and solvent with little or no significant $2F_0-F_C$ density were deleted, until the R_{cryst} and R_{free} values had converged (Table 1).

The CO_2 V143I HCA II structure was similarly refined, but with the addition of dual occupancy refinement of the both bound CO_2 and bicarbonate (Table 1).

Catalysis

The ^{18}O-exchange method relies on the depletion of ^{18}O from CO_2 as measured by membrane inlet mass spectrometry using an Extrel EXM-200 mass spectrometer (18). In the first stage of catalysis, the dehydration of labeled bicarbonate has a probability of labeling the active site with ^{18}O (eq 3). In a following step, protonation of the zinc-bound ^{18}O-labeled hydroxide results in the release of $H_2^{18}O$ to the solvent where it is very greatly diluted by $H_2^{16}O$ (eq 4).

$$HCOO^{18}O^- + EZnH_2O \overset{-H_2O}{\rightleftarrows} EZnHCOO^{18}O^- \rightleftarrows COO + EZn^{18}OH^- \quad (3)$$

$$\mathrm{H}^+ His64-EZn^{18}OH^- \rightleftarrows His64-EZnH_2^{18}O \xrightarrow{\mathrm{H_2O}} His64-EZnH_2O+\mathrm{H_2}^{18}O \quad (4)$$

This approach yields two rates: The R_1, the rate of CO_2 and HCO_3^- interconversion at chemical equilibrium (eq 3), as shown in eq 5, and R_{H2O}, the rate of release from the enzyme of water with labeled substrate oxygen (eq 6).

$$R_1/[\mathrm{E}] = k_{cat}^{exch}[CO_2]/\left(K_{eff}^{CO2}+[CO_2]\right) \quad (5)$$

In eq 5, k_{cat}^{exch} is a rate constant for maximal interconversion of CO_2 and bicarbonate, K_{eff}^{CO2} represents a binding constant for the substrate to enzyme. The ratio $k_{cat}^{exch}/K_{eff}^{CO2}$ is considered equivalent in value to k_{cat}/K_m from steady state experiments, and is a measure of the successful binding and interconversion of substrate and product.

The second rate, R_{H2O}, is the component of the ^{18}O exchange that is dependent upon the donation of protons to the ^{18}O-labeled zinc-bound hydroxide. In such a step, His64 is a predominant proton donor (eq 4) and the value of R_{H2O} can be determined as the rate constant for proton transfer from His64 to the zinc-bound hydroxide according eq 6. Here k_B is the rate constant for proton transfer to the zinc-bound hydroxide and $(K_a)_{donor}$ and $(K_a)_{ZnH2O}$ are ionization constants of the proton donor, His64, and zinc-bound water. The least-squares determination of kinetic constants of eqs 5 and 6 was carried out by using Enzfitter (Biosoft).

$$R_{H2O}/[\mathrm{E}] = k_B/\left(\left[1+(K_a)_{donor}/\left[\mathrm{H}^+\right]\right]\left[1+\left[\mathrm{H}^+\right]/(K_a)_{ZnH2O}\right]\right) \quad (6)$$

The uncatalyzed and carbonic-anhydrase-catalyzed exchanges of ^{18}O between CO_2 and water at chemical equilibrium were measured in the absence of buffer (to prevent interference from intermolecular proton transfer reaction) at a total substrate concentration (all species of CO_2) of 25 mM and 25 °C.

Stopped-Flow Spectrophotometry

Initial rates of CO_2 hydration were determined by measuring the change in absorbance of a pH indicator on an Applied Photophysics SX.18MV stopped-flow spectrophotometer using the method of Khalifah (19). The pK_a value and wavelength for the pH indicator–buffer pair used were *m*-cresol purple ($pK_a = 8.3$), $\lambda = 578$ nm and TAPS. Final buffer concentrations were 25 mM and the pH was 8.3. CO_2 solutions were prepared by bubbling CO_2 into water at room temperature (25°C) at varying CO_2 concentrations. The mean initial rates were measured from 5 to 8 reaction traces comprising the initial 10% of the reaction. Uncatalyzed rates were determined similarly and subtracted from the total observed rates. Determinations of the constants k_{cat} and k_{cat}/K_m were carried out using Enzfitter (Biosoft).

RESULTS

Catalysis

Catalysis by V143I, V143L, and V143A HCA II of the exchange of ^{18}O between CO_2 and water was measured by membrane inlet mass spectrometry. The pH profiles for the catalytic constant $k_{cat}^{exch}/K_{eff}^{CO2}$ (Figure 2) were adequately fit to a single ionization corresponding to the protolysis of the zinc-bound solvent molecule (1-3). Compared with wild-type HCA II, each of the variants had decreased catalytic efficiency as measured by $k_{cat}^{exch}/K_{eff}^{CO2}$ (Table 2). Both mutants V143I and V143L showed sizable decreases in maximal, pH-independent value of $k_{cat}^{exch}/K_{eff}^{CO2}$ by as much as 17-fold. The variant V143A decreased this efficiency about two-fold compared with wild type (Table 2). Changes in the rate constant for proton transfer k_B were two-fold at most (Table 2). The values of the pK_a of the zinc-bound water molecule obtained from the pH profiles of $k_{cat}^{exch}/K_{eff}^{CO2}$ (Figure 2) and $R_{H2O}/[E]$ (Supporting Information, Figure S1) were not significantly altered compared with wild type (Table 2). However, the values of the pK_a of the imidazole side chain of His 64 obtained from pH profiles of $R_{H2O}/[E]$ were decreased slightly for the mutants (Table 2), an effect seen previously in variants of HCA II in which the orientation of the side chain of His64 was inward (20).

The maximal values of the steady-state catalytic constants for hydration of CO_2 were also measured for these variants by stopped-flow spectrophotometry at pH 8.3. These data show the same trend as the ^{18}O exchange data, with k_{cat}/K_m for V143I and V143L decreased up to 20-fold compared with wild type, while the decrease for V143A is near three-fold (Table 3). The values of k_{cat}/K_m determined by stopped-flow should in principle be the same as $k_{cat}^{exch}/K_{eff}^{CO2}$ determined in the ^{18}O-exchange experiments. Comparison of these values in Tables 2 and 3 show values which are similar.

Crystal Structures

Using X-ray crystallography, structures of HCA II variants V143A, V143L and V143I, were solved at 1.70, 1.60, and 1.55 Å resolution, respectively. The structures were refined with final R_{cryst} of < 18% (Table 1). The side chains of each of the substituted amino acids at position 143 faced into the active site, in a manner similar to wild type (Figure 1 and 3). When comparing the overall structures of the three variants with wild type HCA II (PDB: 2ILI) (10), very minor alterations were noticed based on the structural overlay, which showed an average rmsd of 0.19 Å between Cα atoms in the four superimposed models (Figure 4). For the variant V143A HCA II, the size of the CO_2 binding pocket was increased, and two additional ordered solvent molecules (labeled WA and WB in Figure 3A) were observed. These water molecules are not observed in wild type or in the other two variants. In addition to these extra solvent molecules in V143A HCA II, and most likely as a consequence of their presence, the solvent molecule termed "deep water" (DW in Figure 3) appears 2.7 Å away from the oxygen atom of the zinc-bound solvent compared to 2.4 Å for wild type HCA II. In the variant V143L, the deep water appears to have dual occupancy and is shifted 1.0 Å from the zinc (shown as two red spheres labeled DW in Figure 3B).

Substrate and Product Binding in V143I HCA II

Following the procedures of Domsic *et al*, (6) for the entrapment of CO_2 in wild type HCA II, we examined substrate binding in V143I HCA II at a resolution of 0.9 Å. With an rmsd of 0.17 Å between all Cα atoms in wild type and the V143I variant, superimposition shows good structural agreement. Interestingly, both the substrate CO_2 and product bicarbonate were observed in the active site (Figure 5). This is an interesting observation that contrasts with the wild type structure where only CO_2 was observed under these conditions. Hence, careful refinement was performed to determine occupancy of the CO_2 (0.33), the zinc-bound solvent (0.33), and bicarbonate (0.67). Similar to the wild type structure by Domsic et al (PDB ID: 3D92), His64 has a dual inward and outward conformation (21), an unpredictable state when alterations to HCAII have been introduced. Figure 5A and 5B show the calculated omit Fo-Fc electron density map when the CO_2 or bicarbonate were not incorporated into the respective models. This clearly demonstrates the occupancy of both substrate and product (Figure 6).

The CO_2 molecule bound in V143I HCA II is oriented in a side-on conformation similar to that observed by Domsic *et al* (6) (Figure 6A). The CO_2 molecule shows similar spatial orientations in both wild type and V143I HCA II, but with the CO_2 slightly tilted ~10° in the direction of O2 for the latter. The central carbon atom of CO_2 is noticeably closer to the oxygen atom of the zinc-bound water, now 2.5 Å away compared to 2.8 Å for wild type (Figure 7A, Table 4).

The bicarbonate is positioned with O1 and O3 proximal to the CO_2, 1.2 Å away from corresponding oxygen atoms of bound CO_2 (Figure 6B). The other oxygen of the bicarbonate, O2, overlaps with the zinc bound solvent observed in the CO_2 bound form, and coordinates with the zinc, with a distance of 1.9 Å (Figure 6B). Therefore the three oxygen atoms of bicarbonate "mimic" the spatial oxygen atoms of the CO_2 and the zinc bound water. The bicarbonate position observed in V143I HCA II overlaps significantly when superimposed with the previously reported coordinates of bicarbonate bound in HCA II T200H (PDB ID: 1BIC)(22). The rmsd of all Cα atoms in the V143I and T200H HCA II structures with bicarbonate is 0.33 Å (Figure 7B). The V143I mutant has an 18° rotation of bicarbonate toward the O2 atom compared with T200H HCA II. There is also a 0.4 Å separation in carbon atoms between the two superimposed bicarbonate molecules in the T200H and V143I variants.

DISCUSSION

With catalysis nearly diffusion controlled (k_{cat}/K_m at 10^8 $M^{-1}s^{-1}$, (2)) and the binding of CO_2 very weak (K_d near 100 mM, (23)), HCA II may not have a single well-defined enzyme-substrate complex but an array of CO_2 binding modes that leads to catalysis. An aim of this current report is to elucidate the role of the active site configuration in HCA II by perturbing the catalytic binding site of CO_2. Previous work demonstrated that specific replacements of amino acids in the hydrophobic binding pocket of CO_2 are associated with changes in catalytic rates of HCA II (23, 24). Fierke et al. (24) showed decreases in k_{cat}/K_m for hydration of CO_2 associated with the replacement of Val143 at the CO_2 binding site of HCA II by each of nine amino-acids (24).

The variants of HCA II at residue 143 examined in this report make alterations in steric volume of the active-site cavity while avoiding excessive structural perturbations. The replacement of Val143 in wild type (side-chain volume 140 Å^3) by Ile (167 Å^3) and Leu (167 Å^3) demonstrate the effects of decreased steric volume of the cavity and increased hydrophobicity. Val143 was also replaced by Ala (89 Å^3) increasing the volume of the cavity. An overlay of crystal structures of all variants examined in this work showed a superposition of side chain conformations at position 143 with strong side chain overlap in the residues of the active-site cavity, indicating that the unaltered residues in the hydrophobic pocket were not significantly affected by the changes in the volume of the active site (Figure 4). Since these replacements do not impinge on the proposed proton transfer pathway (1), there were rather minor effects on rate constants k_B and k_{cat} that contain contributions of proton transfer between the active site and solvent (Tables 2, 3)(1, 2).

The catalytic efficiency, measured by $k_{cat}^{exch}/K_{eff}^{CO2}$ (Table 2) and k_{cat}/K_m (Table 3), was decreased up to 20-fold for the replacements of Val143 by side chains of larger size (Leu, Ile), and to a much lesser extent with the smaller size (Ala). These data are in rather close agreement with the stopped-flow results of Fierke et al. (24) It is interesting that even increasing the volume of the active-site cavity in V143A HCA II caused a decrease in catalytic activity (Tables 2, 3).

In the active site, the hydrogen bond between the zinc-bound hydroxide and side-chain hydroxyl of Thr199 orients the lone pair electrons of the zinc-bound hydroxyl towards the carbon of CO_2, promoting nucleophilic attack and avoiding an entropic penalty by immobilizing the rotation of the zinc-bound hydroxide about the Zn-O axis (8-10). In the structure of V143I HCAII, the larger side-chain volume of Ile143 compared with Val has forced the carbon atom of bound CO_2 closer to the zinc-bound solvent oxygen by a distance of 0.3 Å (Figure 7A, Table 4). This is associated with a 13- to 17-fold decrease in k_{cat}/K_m and $k_{cat}^{ex}/K_{eff}^{CO2}$ for hydration when V143I is compared with wild type (Tables 2, 3). This sterically crowded active site due to the increased volume of Ile143 is accompanied by the effects of increased hydrophobicity of Ile143 compared with Val143 (estimated at 0.5 kcal/mol based on side chain burial (25)). The overall effect on V143I HCA II is to increase an apparent energy barrier by about 1.7 kcal/mol for catalysis that in wild-type is near 10 kcal/mol. Such an increase could be an effect of the altered active site on the conversion of CO_2 to bicarbonate, or as mentioned below on the the dissociation of product bicarbonate from the active site. This effect is also the case for V143L which shows similar catalytic rates as V143I HCA II (Tables 2, 3).

These explanations must be viewed in the context of the decrease, although smaller in magnitude, of catalytic activity when the active-site cavity is increased in volume in the variant V143A HCA II. Presumably here the position of bound CO_2 is more distant from the zinc-bound solvent than in wild type, reducing the interaction between the unpaired electrons of the oxygen atom of the zinc-hydroxide and CO_2. Work on the binding of CO_2 to V143A HCA II is in progress.

In the crystal structure of V143I HCA II we observed the superimposed occupancy of bicarbonate as well as CO_2 (Figure 5 and 6). There are significant changes in the position of bicarbonate when comparing binding in V143I HCA II and other reports of bound bicarbonate. It is possible that the shifts are due to the larger side chain of isoleucine in V143I HCA II; however, these changes may be indicative of the influence of the experiment. Previous structures with bicarbonate bound (in T200H HCA II (22) and in T199P-C206S HCA II (26)) diffused bicarbonate into crystals, while our data show the appearance of bicarbonate after the reaction of CO_2 and at the active site. Of course, the various replacements in each variant could promote a change in binding that would explain the observed differences in position. Nevertheless, the bicarbonate molecules in each variant bind directly to the zinc, correlating with the catalytic mechanism of direct nucleophilic attack of zinc-bound hydroxide on CO_2.

Using conditions very similar to those reported here, Domsic et al. (6) did not observe bicarbonate in the crystal structure of wild-type HCA II. However, Sjoblom et al. (7) using repeated X-ray exposure did identify bicarbonate bound in HCA II and suggested that bicarbonate formation was a result of enzyme activation due to radiation induced events. This implies that increasing X-ray dose led to enzyme activation perhaps producing active hydroxyl radicals, which would allow for reaction with CO_2 leading to the formation of bicarbonate, as discussed by Sjoblom et al. (7). Radiation damage is a common issue known to impact macromolecular structures under crystallographic conditions, so this behavior between electrons and water molecules is not unlikely (27-30). The absorbed dose at which Sjoblom et al. observed bicarbonate was approximately 6×10^6 Gy, and the occupancies were 65% CO_2 and 35% bicarbonate. In the experiment presented here, the data collection for V143I HCA II maintained a constant radiation dose (estimated radiation dose absorbed at the x-ray beam line used (0.9179 Å wavelength) was 10^6 to 10^7 Gy.), and only one set of data was collected for substrate binding analysis.

The occupancy levels of substrate and product described by Sjoblom et al. are reversed in this study which found 67% bicarbonate and 33% CO_2 at the active site. The higher occupancy of bicarbonate in this study could indicate a change in the product dissociation rate for V143I HCA II. A decrease in the rate of bicarbonate dissociation could explain the higher occupancy of bicarbonate as well as the decrease in k_{cat}/K_m compared with wild type.

Conclusions

Work reported here demonstrates a role for Val143 in the hydrophobic wall providing a productive binding site for CO_2 in HCA II. Replacement of Val143 with Ile resulted in a decrease in the volume of the active site cavity and a resulting shift in which the position of the carbon in bound CO_2 was 0.3 Å closer to the zinc-bound solvent. This was accompanied by a 17-fold drop in catalysis compared with wild type. These results are consistent with the binding of CO_2 to the hydrophobic wall including Val143 as productive in catalysis (3, 24). In fact, Val143 is highly conserved among the carbonic anhydrases in the α class. These data help to develop a possible structure-function relationship between the position of substrate in the enzyme-substrate complex and the catalytic efficiency. Observing specific changes in the binding of substrate related to catalytic activity provides insight into the

catalysis and may provide pathways to variants of carbonic anhydrase with specifically engineered catalytic activity for industrial and environmental uses.

Supplementary Material

Refer to Web version on PubMed Central for supplementary material.

ACKNOWLEDGMENT

ABBREVIATIONS

HCA	human carbonic anhydrase
V143A HCA II	the variant of human carbonic anhydrase with Val143 replaced by Ala
rmsd	root mean squared distance
2XYT	2x Yeast extract and Tryptone

REFERENCES

1. Silverman DN, McKenna R. Solvent-Mediated Proton Transfer in Catalysis by Carbonic Anhydrase. Acc Chem Res. 2007; 40:669–675. [PubMed: 17550224]

2. Lindskog S. Structure and mechanism of carbonic anhydrase. Pharmacol Ther. 1997; 74:1–20. [PubMed: 9336012]

3. Christianson DW, Fierke CA. Carbonic anhydrase: Evolution of the zinc binding site by nature and by design. Accounts of Chemical Research. 1996; 29:331–339.

4. Supuran, CT.; Scozzafava, A.; Conway, J. Carbonic Anhydrase - Its Inhibitors and Activators. CRC Press; Boca Raton: 2004.

5. Chegwidden, WR.; Carter, ND.; Edwards, YH. The Carbonic Anhydrases New Horizons. Birkhauser Verlag; Basel: 2000.

6. Domsic JF, Avvaru BS, Kim CU, Gruner SM, Agbandje-McKenna M, Silverman DN, Mckenna R. Entrapment of Carbon Dioxide in the Active Site of Carbonic Anhydrase II. Journal of Biological Chemistry. 2008; 283:30766–30771. [PubMed: 18768466]

7. Sjoblom B, Polentarutti M, Djinovic-Carugo K. Structural study of X-ray induced activation of carbonic anhydrase. Proc. Natl. Acad. Sci. USA. 2009; 106:10609–10613. [PubMed: 19520834]

8. Merz KM. Co2 Binding to Human Carbonic Anhydrase-Ii. Journal of the American Chemical Society. 1991; 113:406–411.

9. Merz KM. Insights into the Function of the Zinc Hydroxide-Thr199-Glu106 Hydrogen-Bonding Network in Carbonic-Anhydrases. Journal of Molecular Biology. 1990; 214:799–802. [PubMed: 1974931]

10. Fisher SZ, Maupin CM, Budayova-Spano M, Govindasamy L, Tu C, Agbandje-McKenna M, Silverman DN, Voth GA, McKenna R. Atomic crystal and molecular dynamics simulation structures of human carbonic anhydrase II: Insights into the proton transfer mechanism. Biochemistry. 2007; 46:2930–2937. [PubMed: 17319692]

11. Fisher SZ, Tu CK, Bhatt D, Govindasamy L, Agbandje-McKenna M, McKenna R, Silverman DN. Speeding up proton transfer in a fast enzyme: kinetic and crystallographic studies on the effect of hydrophobic amino acid substitution in the active site of human carbonic anhydrase II. Biochemistry. 2007; 42:3803–3813. [PubMed: 17330962]

12. Khalifah RG, Strader DJ, Bryant SH, Gibson SM. C-13 Nuclear Magnetic-Resonance Probe of Active-Site Ionizations in Human Carbonic-Anhydrase B. Biochemistry. 1977; 16:2241–2247. [PubMed: 16641]

13. McPherson, A. Preparation and Analysis of Protein Crystals. Wiley; New York: 1982.

14. Kim CU, Kapfer R, Gruner SM. High-pressure cooling of protein crystals without cryoprotectants. Acta Crystallographica Section D-Biological Crystallography. 2005; 61:881–890.

15. Otwinowski Z, Minor W. Processing of X-ray Diffraction Data Collected in Oscillation Mode. Methods Enzymol. 1997; 276:307–326.

16. Adams PD, Afonine PV, Bunkoczi G, Chen VB, Davis IW, Echols N, Headd JJ, Hung LW, Kapral GJ, Grosse-Kunstleve RW, McCoy AJ, Moriarty NW, Oeffner R, Read RJ, Richardson DC, Richardson JS, Terwilliger TC, Zwart PH. PHENIX: a comprehensive Python-based system for macromolecular structure solution. Acta Crystallographica Section D-Biological Crystallography. 2010; 66:213–221.

17. Emsley P, Cowtan K. Coot: model-building tools for molecular graphics. Acta Crystallogr. 2004; D60:2126–2132.

18. Silverman DN. Carbonic anhydrase: oxygen-18 exchange catalyzed by an enzyme with rate-contributing proton-transfer steps. Methods Enzymol. 1982; 87:732–752. [PubMed: 6294458]

19. Khalifah RG. Carbon Dioxide Hydration Activity of Carbonic Anhydrase.1. Stop-Flow Kinetic Studies on Native Human Isoenzyme-B and Isoenzyme-C. Journal of Biological Chemistry. 1971; 246:2561–2573. [PubMed: 4994926]

20. Mikulski RL, Silverman DN. Proton transfer in catalysis and the role of proton shuttles in carbonic anhydrase. Biochimica Et Biophysica Acta-Proteins and Proteomics. 2010; 1804:422–426.

21. Nair SK, Christianson DW. Unexpected pH-Dependent Conformation of His-64, the Proton Shuttle of Carbonic Anhydrase-II. Journal of the American Chemical Society. 1991; 113:9455–9458.

22. Xue YF, Vidgren J, Svensson LA, Liljas A, Jonsson BH, Lindskog S. Crystallographic Analysis of Thr-200 -] His Human Carbonic-Anhydrase Ii and Its Complex with the Substrate, Hco3- Proteins-Structure Function and Genetics. 1993; 15:80–87.

23. Krebs JF, Rana F, Dluhy RA, Fierke CA. Kinetic and Spectroscopic Studies of Hydrophilic Amino-Acid Substitutions in the Hydrophobic Pocket of Human Carbonic Anhydrase-Ii. Biochemistry. 1993; 32:4496–4505. [PubMed: 8485128]

24. Fierke CA, Calderone TL, Krebs JF. Functional Consequences of Engineering the Hydrophobic Pocket of Carbonic Anhydrase-Ii. Biochemistry. 1991; 30:11054–11063. [PubMed: 1657158]

25. Karplus PA. Hydrophobicity regained. Protein Science. 1997; 6:1302–1307. [PubMed: 9194190]

26. Huang S, Sjoblom B, Sauer-Eriksson AE, Jonsson BH. Organization of an efficient carbonic anhydrase: Implications for the mechanism based on structure-function studies of a T199P/C206S mutant. Biochemistry. 2002; 41:7628–7635. [PubMed: 12056894]

27. Borek D, Cymborowski M, Machius M, Minor W, Otwinowski Z. Diffraction data analysis in the presence of radiation damage. Acta Crystallographica Section D-Biological Crystallography. 2010; 66:426–436.

28. Ravelli RBG, Garman EF. Radiation damage in macromolecular cryocrystallography. Current Opinion in Structural Biology. 2006; 16:624–629. [PubMed: 16938450]

29. Carugo O, Carugo KD. When X-rays modify the protein structure: radiation damage at work. Trends in Biochemical Sciences. 2005; 30:213–219. [PubMed: 15817398]

30. Sippel KH, Genis C, Govindasamy L, Agbandje-McKenna M, Kiddle JJ, Tripp BC, McKenna R. Synchrotron Radiation Provides a Plausible Explanation for the Generation of a Free Radical Adduct of Thioxolone in Mutant Carbonic Anhydrase II. Journal of Physical Chemistry Letters. 2010; 1:2898–2902. [PubMed: 20976122]

31. Steiner H, Jonsson BH, Lindskog S. Catalytic Mechanism of Carbonic-Anhydrase - Hydrogen-Isotope Effects on Kinetic-Parameters of Human C Isoenzyme. European Journal of Biochemistry. 1975; 59:253–259. [PubMed: 1249]

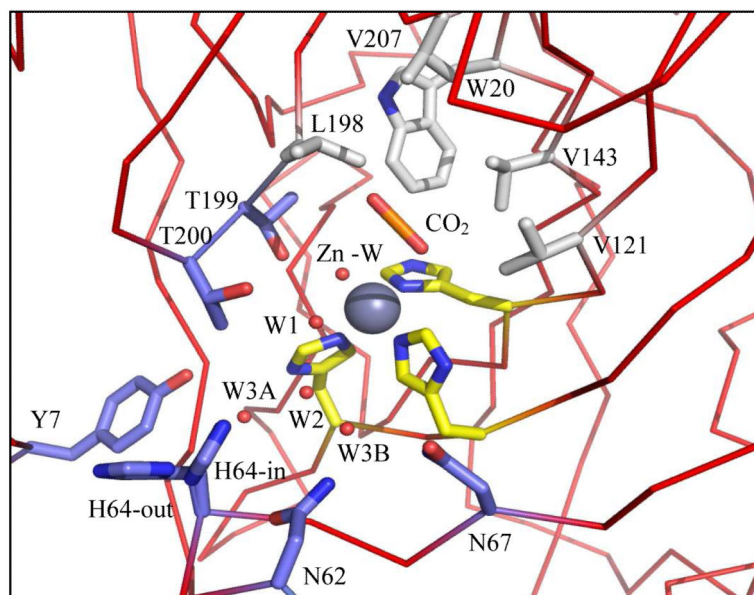32. DeLano, WL. The PyMOL Molecular Graphics System. DeLano Scientific; San Carlos, CA, USA: 2002. http://www.pymol.org

Figure 1.
Stick diagram of the active site of HCA II. Substrate CO_2 (orange), active site solvent (red spheres), hydrophobic pocket (light gray), the hydrophilic region (blue), and the three histidines (yellow) stabilizing the zinc (dark gray). PDB ID: 2ILI (10). Amino acids are as labeled. This figure was generated with PyMol (32).
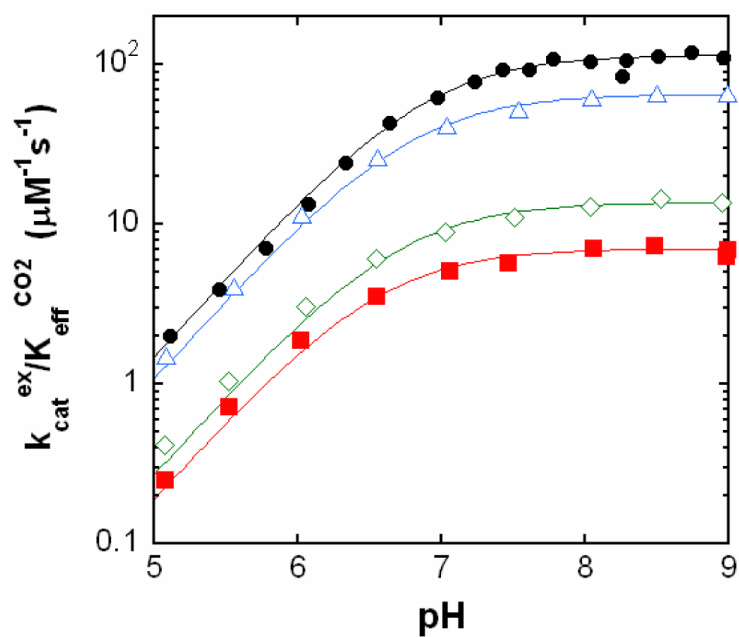
Figure 2.
pH profiles of $k_{cat}^{ex}/K_{eff}^{CO2}$ (μM^{-1} s^{-1}) for the hydration of CO_2 catalyzed by variants of HCA II: wild type (black, ●); V143A (blue, △); V143I (red, ■); and V143L (green, ◇). Data were obtained from rates of depletion of ^{18}O from CO_2 measured by membrane inlet mass spectrometry at 25 °C in solutions containing 25 mM ^{18}O-enriched CO_2/bicarbonate. No buffers were added.
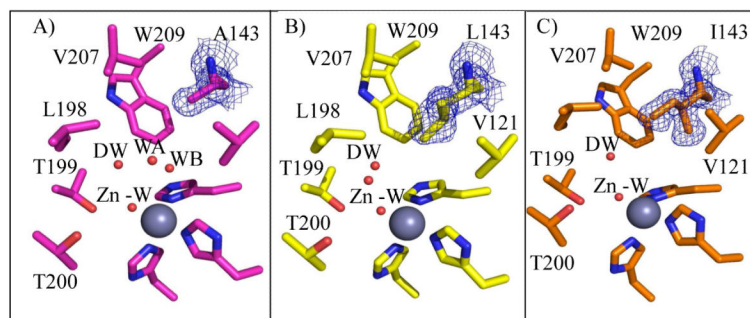
Figure 3.
Crystal structure at the active-site of the A) V143A (pink), B) V143L (yellow), and C) V143I HCAII (orange). Amino acids are as labeled. Shown are the calculated $2F_o$-F_c electron density map for the 143 position, contoured at 1.5σ (blue). Solvent molecules are depicted as red spheres and the three histidines coordinating the zinc (dark gray). This figure was generated with PyMol (32).
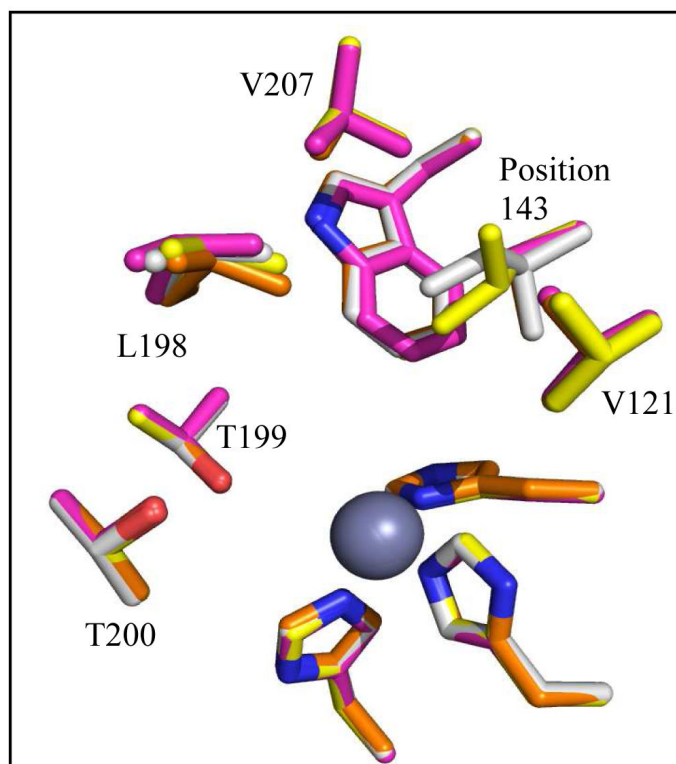
Figure 4.
Stick overlay of position 143 HCA II structures. Wild type (orange), V143A (pink), V143L (yellow), and V143I HCAII (white). Amino acids are as labeled. In addition the three histidines coordinating the zinc (dark gray) are shown. This figure was generated with PyMol (32).
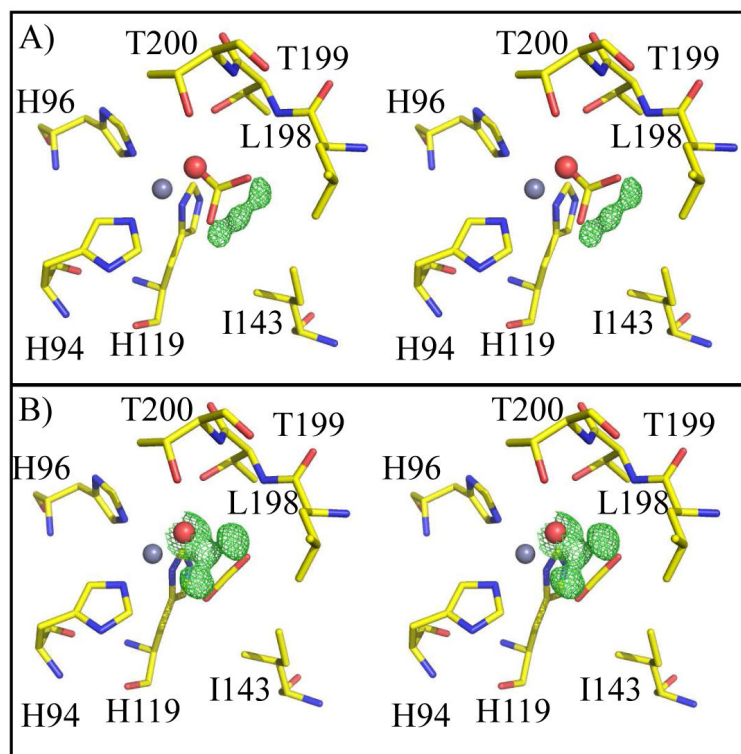
Figure 5.
Stick stereo figure of the active site of V143I HCA II CO_2/bicarbonate complex. Shown are the calculated omit Fo-Fc electron density map, contoured at 3σ (green), when the A) CO_2 and B) bicarbonate were not incorporated into the respective models. The residual electron density in either case indicates presence of both substrate and product. Amino acids are as labeled. This figure was generated with PyMol. (32).
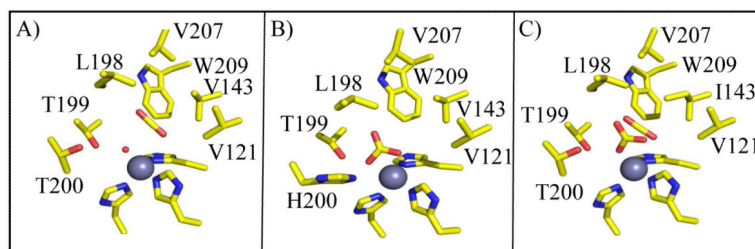
Figure 6.
Structure of substrate/product bound in HCAII V143I. A) CO_2 and H_2O molecules (red sphere), B) HCO_3^-, and C) as observed in the crystal structure, with dual occupancy (Refer to Figure 5). Amino acids are as labeled. This figure was generated with PyMol (32).
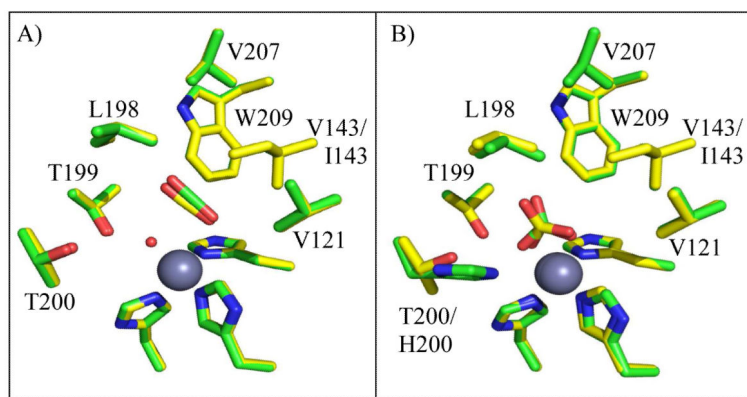
Figure 7.
Comparison of HCA II V143I substrate and product binding in HCA II. Structural overlay
A) of CO_2 binding in wild type (green) (6) and V143I (yellow) HCAII, B) of bicarbonate
binding in T200H (green) (21) and V143I (yellow). Amino acids are as labeled. This figure
was generated with PyMol (32).

Table 1

Data processing and refinement statistics for the structures of the HCA II variants

Parameter	V143A	V143I	V143L	V143I (CO$_2$ bound)
PDB code	3U3A	3U45	3U47	3U7C
Space group	P2$_1$	P2$_1$	P2$_1$	P2$_1$
Cell dimensions a, b, c (Å) β (°)	42.3, 41.6, 72.3 104.4	42.2, 41.3, 72.1 104.2	42.3, 41.6,72.3 104.5	42.3,41.5, 72.1 104.2
Resolution (Å)	20-1.7(1.76-1.70)*	20-1.55(1.61-1.55)	20-1.60(1.66-1.60)	20-0.93(0.95-0.93)
R$_{sym}$ [b] (%)	3.7(9.4)	4.8(8.8)	4.4(9.1)	8.2(44.7)
I/sigma(I)	28.1(12.8)	28.1(4.9)	35.9(5.8)	22.3(2.4)
Completeness (%)	96.7(98.1)	90.0(85.4)	90.7(96.9)	97.2(85.9)
Average Redundancy	3.3(3.2)	4.6(4.6)	3.2(3.1)	5.9(3.2)
Number of unique reflections	26105	31566	29306	157750
R$_{cryst}$ [c]/R$_{free}$ [d] (%)	16.0/19.1	16.2/19.3	17.9 / 21.1	10.6/13.1
No. atoms - Protein[#]	2090	2120	2062	2237
Water	287	248	288	546
B-factors (Å^2)				
Protein (main/side)	13.2/17.4	13.7/17.1	13.3/16.6	8.4/11.3
Water	24.8	24.3	25.1	31.9
RMSD (bond (Å)/angle(°))	0.006/1.092	0.006/1.127	0.006/1.034	0.014/1.031
Ramachandran plot (%)				
Favored	96.9	97.4	96.5	87.1
Allowed	3.1	2.7	3.1	12.9
Outliers	0.0	0.0	0.4	0.0

[a]Values in parentheses are for the highest resolution shell.

[b]R$_{sym}$ = $(\Sigma|I - <I>|/ \Sigma<I>) \times 100$.

[c]R$_{cryst}$ = $(\Sigma||F_O| - |F_C||/ \Sigma|F_0|) \times 100$.

[d]R$_{free}$ is calculated the same as R$_{cryst}$, except with 5% of the data omitted from refinement.

*Indicates statistics in the last resolution bin.

[#]Number of atom varies because of observed duel conformations of side-chains.

Table 2

Maximal values of rate constants for the hydration of CO_2 and dehydration of bicarbonate catalyzed by variants of HCA II, and related pK_a values, obtained by ^{18}O exchange at 25 °C.

Variant	$k_{cat}^{exch}/K_{eff}^{CO2}$ ($\mu M^{-1} s^{-1}$)	pK_{ZnH2O} [a]	k_B (μs^{-1})	pK_{ZnH2O} [b]	pK_{donor} [b]
Wild-type [c]	120	6.9	0.8	6.8	7.2
V143A	65 ± 6 [d]	6.8	1.4 ± 0.3 [d]	6.6	6.6
V143I	7.1 ± 0.2	6.6	0.4 ± 0.1	6.4	6.7
V143L	14 ± 1	6.7	$0.7 \pm .04$	6.5	6.5

[a] Obtained from the pH profile of $k_{cat}^{exch}/K_{eff}^{CO2}$. The standard errors here are ± 0.1.

[b] Obtained from the pH profiles of R_{H2O}. The standard errors here are ± 0.1 to ± 0.2.

[c] From Fisher et al. (11)

[d] Standard errors were determined from ^{18}O-exchange data as in Figures 2 and S1.

Table 3

Steady-state constants for catalysis of the hydration of CO_2 by variants of HCA II obtained by stopped-flow spectrophotometry at 25 °C and pH 8.3.

Variant	k_{cat}/K_m ($\mu M^{-1}s^{-1}$)	k_{cat} μs^{-1})
Wild-type[a]	120	1.0
V143A	42 ± 1[b]	0.5 ± 0.2[b]
V143I	9.3 ± 0.3	0.7 ± 0.1
V143L	5.5 ± 0.1	1.1 ± 0.3

[a]From Steiner et al. (31)

[b]Standard errors were determined from fits of steady-state data.

Table 4

Interatomic distances in Å for CO_2 in HCA II and variants. Distances for CO_2 atoms are measured from substrate atoms to the oxygen atom of the zinc-bound solvent.

Atoms of CO_2	Wild type[a]	Wild type[b]	V143I[c]
C	2.8	2.8	2.5
O_1	3	2.8	2.8
O_2	3.1	3.1	2.7

[a]Ref (6)

[b]Ref (7)

[c]This work. The uncertainty in these distances is 0.1 Å.